Exploring Phase Transitions and Magnetoelectric Coupling of Epitaxial Asymmetric Multilayer Heterostructures

Exploring Phase Transitions and Magnetoelectric Coupling of Epitaxial Asymmetric Multilayer Heterostructures

Dhiren K. Pradhan[1,2*], Shalini Kumari[3], Venkata S. Puli[4], Dillip K. Pradhan[5], Ashok Kumar[6], Sergei V. Kalinin[2], Rama K. Vasudevan[2], Ram S. Katiyar[7], Philip D. Rack[1,2*]

[1]Department of Materials Science & Engineering, University of Tennessee, Knoxville, Tennessee 37996, USA.
[2]Center for Nanophase Materials Sciences, Oak Ridge National Laboratory, Oak Ridge, Tennessee 37831, USA.
[3]Department of Materials Science & Engineering, The Pennsylvania State University, University Park, Pennsylvania 16802, USA.
[4]Department of Chemistry, Federal University of São Carlos, São Carlos, São Paulo 13565-905, Brazil.
[5]Department of Physics & Astronomy, National Institute of Technology, Rourkela-769008, India.
[6]National Physical Laboratory (CSIR), New Delhi 110012, India.
[7]Department of Physics and Institute of Functional Nanomaterials, University of Puerto Rico, San Juan, PR 00936, USA.

Abstract

Magnetoelectric (ME) heterostructures can exhibit magnetic and ferroelectric ordering temperatures with large ME coupling at room temperature (RT) compared to the single-phase multiferroic materials. We synthesized $Pb(Fe_{0.5}Nb_{0.5})O_3(PFN)/Ni_{0.65}Zn_{0.35}Fe_2O_4(NZFO)/Pb(Fe_{0.5}Nb_{0.5})O_3(PFN)/Ni_{0.65}Zn_{0.35}Fe_2O_4(NZFO)/Pb(Fe_{0.5}Nb_{0.5})O_3(PFN)$ multilayer heterostructures having dimensions 40/10/40/10/40 nm. High quality epitaxial growth of these heterostructures has been confirmed via X-ray diffraction (XRD) and selected area electron diffraction patterns (SAED). These nanostructures show well saturated polarization (~ 52 $\mu C/cm^2$) and magnetization (~ 62 emu/cm^3) at RT. The magnetic and ferroelectric transitions occur well above RT. These heterostructures exhibit relaxor behavior and undergo a 2nd order ferroelectric phase transition. Magnetodielectric measurements show significant coupling between the magnetic and electrical order parameters at RT. These characteristics of these heterostructures make them suitable as potential candidates for ultra-low power memory, spintronics, and different multifunctional (micro)nanoscale device applications.

*Authors to whom correspondence to be addressed. Electronic mail: dhirenkumarp@gmail.com (Dhiren K. Pradhan), prack@utk.edu (Philip D. Rack).

Introduction

Multiferroic (MF) materials are an important class of multifunctional materials which exhibit two or more primary ferroic orderings such as ferroelectricity, ferro(antiferro/ferri) magnetism, ferroelasticity, and ferrotoroidicity in the same phase.[1-5] The coexistence of ferroic order parameters lead to cross coupling between them so that one ferroic property can be controlled and switched with the conjugate field of the other. The coupling between the magnetic and ferroelectric orderings is known as magnetoelectric (ME) coupling which is very important in terms of fundamental physics and device application point of view.[1-6] This coupling permits the control and switching of magnetization by an electric field and ferroelectric polarization by a magnetic field.[1, 2, 6] The quest for ME materials operated at room temperature remains of keen interest for their potential applications in ideal ultralow power and high-density memory, spintronics, magnetic field sensors, and other multifunctional devices.[6-11] Electric and magnetic properties of solids are usually considered independently as magnetism is related to spins and orbital motions of electrons, whereas ferroelectricity results from ion displacements and center of gravity of electrons.[1, 2, 12, 13] Despite the apparent incompatibility between the magnetic and electrical properties, some families of materials exhibit multiferroicity in a single phase.[1, 12] The single-phase materials discovered to date have magnetic transition temperatures below room temperature and lead to lower ME coupling. Other room temperature single phase multiferroics exist in nature have higher leakage current and thus lower ME coupling.[1, 2, 14, 15] Recently Intel designed magnetoelectric spin orbit (MESO) logic device which operates via ME effect and inverse Rashba–Edelstein effect. This device exhibits 10 to 30 times higher switching energy, 5 times lower switching voltage and 5 times higher logic density than the current CMOS based devices. In this MESO logic devices.[6, 9] $Bi_{1-x}La_xFeO_3$ has been used as multiferroic material, which has several drawbacks such as high leakage current and low ME coupling at RT.[16] Hence the drive to search for suitable ME material with large ME coupling at RT continues. To observe robust ME coupling and higher operating temperature (T_C) above room temperature ME composites have been envisioned. [14, 15, 17-19]

Different systems such as (i) ferroelectric (FE) - ferromagnetic (FM) /antiferromagnetic (AFM)/ferrimagnetic composites (ii) MF-FE composites, (3) MF-MF, and (4) MF-FM/AFM/Ferrimagnetic composites have been designed to produce strong ME coupling at RT.[14, 15, 17-19] In 1972 van Suchtelen reported that in MF composites, ME coupling is a product tensor property, which arises from the interaction among the order parameters of the constituent phases.[20] By appropriate design of different composite architectures such as: (i) FE-FM particulate composites (ii) FE and FM horizontal multilayer heterostructures (iii) vertical

nanostructures (magnetic nanorods in FE matrix) (iv) hybrid composite structures, ME coupling and other functionalities can be tailored.[14, 19, 21] Among the above composite architectures, epitaxial MF oxide multilayer heterostructures having alternate FE and FM layers with atomically sharp interfaces can lead to large ME coupling and enhanced functionalities.[22-25] Multiple interfaces in oxides can provide unique opportunities for the coupling between spin, charge, lattice, and orbital degrees of freedom, which can lead to new functional properties and quantum states.[14, 22-31] While choosing the FE and magnetic candidates for heterostructures, priority should be given to the chemical stabilities and their behavior at the interface to prevent intermixing that may lead to decreasing of the coupling between the order parameters.[14, 22, 32, 33] The large ME coupling observed in heterostructures is due to the cross interaction between the FE and magnetic phases via (i) lattice strain (ii) exchange bias (spin exchange) and (iii) charge coupling (interfacial electronic reconstruction).[15, 19, 22-24, 29, 34, 35] In strain-mediated ME coupling, the FE material induces strain through piezoelectric and/electrostrictive effects, and the induced strain transmits to the magnetic phase. The developed strain in the magnetic component modulates the magnetic order parameters and magnetic anisotropy via piezomagnetism and/magnetostriction.[14, 19, 29, 36] ME coupling due to spin exchange, so called exchange bias effect, couple the spins of a FM and the uncompensated AFM multiferroic at the interface.[6, 15, 22, 24, 37,34] In charge-mediated ME coupling, the bound charge at the FE interface modulate the charge carrier density of the magnetic layer via a field effect.[22, 24, 25, 35] The magnetic order parameters can also be tuned by suitable modification of (i) the magnetic anisotropy (due to spin-orbit coupling) (ii) magnetization (local spin amplitude) and (iii) exchange constant.[22-25,30] When choosing the materials for ME composites, the FE candidate should have high FE transition temperature, high polarization, high piezoelectric (electrostriction) coefficients, low loss tangent and the magnetic material should exhibit high magnetic curie temperature, high magnetization, high piezomagnetic (magnetostriction) coefficient with high resistivities.[15, 19, 22-24, 29]

Various experimental and theoretical studies have been reported that exhibit strong ME coupling for several thin film heterostructures. Different heterostructures such as $BiFeO_3$/$La_{0.7}Sr_{0.3}MnO_3$ bilayer, $Ni_{0.5}Mn_{0.35}In_{0.15}$/$Pb_{0.96}La_{0.04}(Zr_{0.52}Ti_{0.48})O_3$ bilayer, Ni/$Pb(Mg_{1/3}Nb_{2/3})O_3$–$PbTiO_3$ (PMN-PT) bilayer, $PbZr_{0.57}Ti_{0.43}O_3$/$NiFe_2O_4$ bilayer, PFN/NZFO/PFN trilayer, $PbZr_{0.57}Ti_{0.43}O_3$/$CoFe_2O_4$ multilayers, $BaTiO_3$/$BiFeO_3$/$BaTiO_3$ trilayer, $PbZr_{0.2}Ti_{0.8}O_3$/$La_{0.8}Sr_{0.2}MnO_3$ multilayers, $Ba_{0.7}Sr_{0.3}TiO_3$/$La_{0.7}Sr_{0.3}MnO_3$ multilayers and superlattices, and $BaTiO_3$/$CoFe_2O_4$ multilayers show strong ME coupling and operate above RT.[22, 29, 34, 37-45]

To induce strong ME coupling above RT, we have grown asymmetric epitaxial multilayer heterostructures of PFN/NZFO/PFN/NZFO/PFN. Because multiple interfaces in oxide heterostructures can provide outstanding opportunities for the coupling between spin, charge, lattice, and orbital degrees of freedom, which can lead to new functional properties and quantum states. [14, 22-31] In these asymmetric heterostructures, the NZFO ($\sim$ 10 nm) layer are kept much thinner than the PFN (40 nm) layer to minimize the leakage current and to withstand high electric field as NZFO is less resistive than PFN. The epitaxial nature with well-defined interfaces of MF and FM layers should lead to strong ME coupling between the FE and magnetic layers due to high mechanical strain transmission. PFN is chosen as the bulk ceramics of PFN exhibits FE T_C above RT (379-385 K), high dielectric permittivity, low dielectric loss with interesting ferroelectric, piezoelectric, magnetic, and ferroelastic properties. [18, 29,46, 47] NZFO is chosen as the bulk ceramics of NZFO has a magnetic $T_C \sim$ 663 K, high magnetization and magnetostriction, low leakage current with good structural, chemical, and thermal stability.[18, 29, 48-50] The physical properties of PFN and NZFO ceramics in detail have been reported elsewhere.[18, 29, 48-50] PFN thin film shows a ferroelectric $T_C \sim$ 400 (+/- 5) K, and weak ferromagnetic/antiferromagnetic ordering with excellent piezoelectric and ferroelectric(saturation polarization (P_s) $\sim$ 57 $\mu C/cm^2$) properties at RT. [50, 51] NZFO thin films exhibit a magnetic $T_C \sim$ 710 K with large saturation magnetization and low coercive filed at RT. [52]Hence, strong ME coupling, enhanced ferroelectric and magnetic properties with both the T_C well above RT can be realized in these multilayer heterostructures.

Here we report the structural, morphology, scanning transmission electron microscopy (STEM), piezoresponse force microscopy (PFM), dielectric, ferroelectric, magnetic, and ME properties of the above mentioned multilayer heterostructures.

Experimental Details

We synthesized 1-inch diameter PFN and NZFO ceramic targets by standard solid-state reaction methods. The detailed synthesis procedure, conditions and other physical properties of both the compounds are reported elsewhere.[48, 49] PFN/NZFO/PFN/NZFO/PFN asymmetric multilayer heterostructures were synthesized on LaNiO$_3$ buffered LSAT ((LaAlO$_3$)$_{0.3}$ (Sr$_2$AlTaO$_6$)$_{0.7}$) substrates by pulsed laser deposition (PLD) having an excimer KrF laser of wavelength $\sim$ 248 nm. First, we grew a 70 nm layer of LaNiO$_3$ at 700 °C in an oxygen partial pressure of 200 mTorr then annealed these films at 700 °C for 30 minutes in

300 Torr of oxygen atmosphere. Each PFN and NZFO layer was grown at 600 °C at an oxygen partial pressure ~ 20 mTorr and ~ 150 mTorr, respectively; oxide growth under a modest oxygen partial pressure is necessary to maintain the oxygen stoichiometry. The energy density of the laser was kept fixed ~ 1.5 J/cm^2 during the deposition of both layers. Finally, the multilayer heterostructures were annealed at 700° C for 30 minutes in 300 Torr oxygen and then cooled to RT. Each layer of PFN and NZFO were confirmed to be 40 and 10 nm, respectively, with a total heterostructure thickness of ~ 140 nm.

The phase formation and phase purity of PFN/NZFO/PFN/NZFO/PFN heterostructures were examined by using high resolution XRD with CuK_α radiation (λ = 1.5405 Å). The XRD patterns were captured at a scan rate of 0.5 °/min in a wide scan angle (2θ) of 20-80°. Then we measured the thickness of the heterostructures using a profilometer (XP-200) and Scanning Transmission Electron Microscopy (STEM). For STEM imaging, we prepared the lamellae from the heterostructure using Focused ion beam (FIB). Then the lamellae were transferred to a 3 mm copper-mesh grid coated with carbon using a glass needle along with a micromanipulator using an optical microscope. Images of the multilayer heterostructures were recorded utilizing a STEM (Philips CM 200 (FEG)) operated ~ 200 kV using a HAADF (high-angle annular dark-field) detector. We performed Piezoresponse Force Microscopy (PFM) measurements on the heterostructures to check the domain structure and observe electrotechnical switching. The frequency dependence of piezoresponse of the sample was measured by Band Excitation (BE) technique.[53] The heterostructures were pasted on a circular metallic plate by using silver paint, which act as bottom electrode for the experiments and was grounded. All the PFM measurements were carried out using cantilevers (Budget Sensors ElectriMulti75- G) having force constant (k) ~ 1 N/m with a free resonance of ~75 kHz with a multimode atomic force microscope (Veeco) assembled with a Nanonis SPM controller. Data Acquisition (DAQ) cards (National Instruments) were used for the acquisition and generation of signal and for the BE experiments. All the PFM experiments were performed at a fixed ac voltage amplitude of ~ 3 V, whereas the scanning voltage used for the hysteresis measurements ranges from -10 V to +10 V. All the PFM measurements were carried out in a wide frequency range of 260-360 kHz with a central frequency of ~ 310 kHz. For dielectric and ferroelectric measurements, Pt top electrodes of thickness ~ 40 nm and area ~ 80 μm^2 were deposited by DC sputtering. Temperature dependent dielectric properties were measured at different frequencies (1 kHz – 1 MHz) in a large temperature range (200 - 700 K) utilizing an HP4294A impedance analyzer at a fixed ac voltage amplitude of ~ 100 mV. The temperature

was precisely controlled with the help of a programmable controller (MMR K-20). Electric field dependent polarization (P-E hysteresis) loops were recorded at RT using a ferroelectric tester (Radiant Technologies Inc.). We performed the temperature and magnetic field dependence of dc magnetization measurements of these heterostructures with a Dynacool physical property measurement system (PPMS). Magnetodielectric measurements were performed utilizing a vibrating sample magnetometer (VSM) and an HP4294A impedance analyzer.

Results and discussion

Structural Characterization

The schematic diagram of PFN /NZFO/PFN/NZFO/PFN multilayer heterostructures is shown in Fig. 1(a).

First, we examined the crystallinity, phase purity, and crystal structure of PFN /NZFO/PFN/NZFO/PFN multilayer heterostructures grown on LNO deposited LSAT substrate by recording XRD pattern at RT (Fig. 1(b)). PFN, NZFO, and LSAT/LNO (overlapped) diffraction peaks are assigned with symbols *, $, and #, respectively. The XRD pattern exhibits the presence of only the (00l) diffraction peaks of substrate, LNO, PFN, and NZFO in a wide range of X-ray scans angle (20- 80°) indicating that these heterostructures are highly c-axis oriented in nature. The epitaxial nature of the heterostructures will be discussed in Transmission Electron Microscopy (TEM) section. There are no secondary phases and pyrochlore phases (which occurs due to lead deficiency) in the XRD pattern confirming the growth of phase pure samples. PFN and NZFO diffraction peaks correspond the monoclinic and cubic (inverse spinel) crystal structure, respectively.[54] We have computed the effective strain of the heterostructures at different interfaces, as strain can strongly influence the physical properties including ME coupling. The LSAT substrate has the lattice parameter (a) ~ 3.868 Å with cubic crystal structure and LNO has a= 3.838 Å. The effective misfit strain (ε) due to LNO on LSAT is found to be ~ 0.78 % (in-plane tensile strain). The lattice parameter of NZFO is ~ 8.368 Å, hence it is possible that it sits on the top of four unit cells of PFN (a= 4.015 Å) while the growth of NZFO on PFN and four unit cell of PFN on one unit cell of NZFO during the growth of PFN on NZFO.[52, 54] We carefully checked the diffraction peak positions of PFN and NZFO in this XRD pattern and compared to their respective bulk peaks. We found that all the PFN peaks in the heterostructures are shifted towards lower angle whereas the NZFO (400)

peak is shifted towards lower angle compared to their stress-free bulk 2θ values. PFN and NZFO layers experiences effective misfit strain of ~ 0.66 % and 0.22 %, respectively. In addition to these strains, these heterostructures exhibit different compressive and tensile strains at different interfaces in these heterostructures including the substrate and bottom electrodes.[36]

TEM Studies

TEM is a useful technique to obtain structural and spectroscopic information of various heterostructures fabricated by two or more different materials, and the atomic mismatch, orientation or substitution in the interlayer at the atomic level.[23, 28, 30, 35, 55] Therefore, TEM was used in this study to collect the information on the crystal structure, local chemical composition , and strain distribution. [23, 28, 30, 35, 55] Detailed EDS analysis was also done using the TEM (Fig. S2 in the supplementary material). The cross-sectional samples of the PFN/NZFO/PFN/NZFO/PFN heterostructure was cut across the center of the structure using a focused ion beam. Fig. 2(a) is a cross-sectional high resolution TEM image of a (00*l*) - oriented PFN/NZFO/PFN/NZFO/PFN heterostructures deposited on LSAT substrates along with LNO buffered layer, wherein the PFN and NZFO layers appear as dark and bright bands, respectively. The cross-sectional TEM image recorded at higher resolution is also shown in Fig. S1 (supplementary material). The thickness of the individual layers was measured, and the heterostructures exhibit two ~10 nm NZFO layers sandwiched between three ~ 40 nm PFN layers with a total film thickness of ~ 140 nm. Both oxide layers in this heterostructure showed excellent crystallinity and sharp interfaces with no sign of any amorphous interfacial layers. The SAED patterns were recorded corresponding to five layers shown in Fig. 2(b) and confirms the epitaxial growth of the layers along (00l) direction consistent with the XRD data. From the SAED pattern, the lattice spacing for PFN and NZFO were computed and found to be well matched with the values calculated from the XRD pattern. STEM-EDS were utilized to study the chemical composition of all individual elements in the heterostructure (Fig. S2 in the supplementary material).

Scanning Probe Microscopic Studies

We examined the surface morphology to probe the quality of thin film growth of the PFN/NZFO/PFN/NZFO/PFN heterostructures by capturing the Atomic Force Microscopy (AFM) images on a ~ 3 × 3 μm^2 scanning area in a contact mode at RT (Fig. 3 (a)). The surface of these heterostructures are observed to be homogeneous and smooth without any

microcrack/holes and the grains are densely packed. We observed the average roughness around 1.5 nm.

We carried out the PFM spectroscopy experiments of the PFN/NZFO/PFN/NZFO/PFN heterostructures to study the polarization switching and ferroelectricity at the nanoscale (Fig. 3(b,c,d)).[56, 57] PFM measures the strain (electromechanical response) of the FE materials utilizing the piezoelectric effect when a dc voltage and an ac excitation voltage is applied to the AFM. Fig. 3(b) shows a 8×8 μm^2 PFM phase image after poling with a probe bias of +6 V over a 3×3 μm^2 and -6 V over a 5×5 μm^2. It can be clearly seen that the PFM phase reversal after poling is 180°. The negative and positive poled area show significant and reversible phase contrast (out-of-plane) above ± 6 V which suggests re-orientation of the ferroelectric polarization. The observed phase inversion in this case by applying DC bias could not be ruled out because of the local surface charging due to injection of charge along with electrostatic forces on the tip, which in turn shifts the electrostatic forces on the voltage axis.[53, 56, 58] We examined the phase of negative and positive poled area and observed the phase flipping, which indicates that the observed effect is intrinsic. We also measured the phase and amplitude loops as a function of DC bias (Fig. 3(c)). We observed a 180° phase flipping in the phase hysteresis loop and butterfly amplitude loops with its minimum at ~ ± 5 V (coercive field); these signatures suggest these heterostructures are ferroelectric. To further elucidate the polarization switching characteristics of the poling experiments is not due to extrinsic effects, piezoresponse measurements were done as a function of tip voltage in the on-field (when the V_{DC} on) and off-field (immediate after switching off V_{DC}) modes shown in Fig. 3(d). We observed significant piezoresponse in both the regimes. We calculated the values of coercive fields (V_+, V_-) and remanent piezoresponse (R_+, R_-) from the off-field piezoresponse loop measured for cycle 2 and found them to be $V_+ \sim$ + 5.56 V, $V_- \sim$ - 3.95 V, $R_+ \sim$ 0.68, and $R_- \sim$ 0.54. This observation coupled with poling experiments suggests the existence of intrinsic ferroelectric behavior in our heterostructures and shows that there is a monodomain structure. We also performed bulk characterization techniques to further confirm the ferroelectric character as explained below.

Dielectric and Ferroelectric Properties

We performed temperature dependent dielectric measurements at different frequencies to probe the ferroelectric ordering temperature, nature of ferroelectric transition, and loss tangent of the PFN/NZFO/PFN/NZFO/PFN heterostructures (Fig. 4(a,b)). The typical polar dielectric nature of the material has been observed where the dielectric permittivity decrease with increase in the frequencies.[59] The dielectric permittivity slowly increases with temperature up to 450 K,

then increases rapidly up to the ferroelectric T_C (phase transition temperature) then decreases with further increase in the temperature. The temperature dependent dielectric spectra show broad maxima (except 1 kHz) along with the frequency dependent dielectric dispersions (Fig. 4(a)). These heterostructures exhibit diffuse phase transition behavior, moreover the diffuseness of the phase transition increases with increase of frequency. The ferroelectric T_C is found to shift towards higher temperatures with an increase of frequency and the dielectric spectra above the T_C merge with each other regardless of the frequency. This temperature dependent dielectric behavior is typical for relaxor type ferroelectrics.[60, 61]

From the temperature dependent dielectric spectra, the diffuseness of ferroelectric phase transition can be explained using modified form of Curie - Weiss law represented by [60, 62]

$$\frac{1}{\varepsilon_r} - \frac{1}{\varepsilon_m} = \frac{(T - T_c)^\gamma}{C} \qquad (1)$$

$$C = 2\varepsilon_m \, \delta^\gamma \qquad (2)$$

Where ε_r= dielectric permittivity, C= Curie constant, T_o= Curie temperature, T = absolute temperature, T_C = ferroelectric phase transition temperature, ε_m= maximum value of dielectric permittivity at T_C, C= modified Curie Wiess constant, δ = diffuseness parameter and γ = degree of diffuseness. The value of γ generally varies from 1 to 2, for normal ferroelectrics γ=1, whereas for relaxor ferroelectrics γ value is close to 2.[60, 62, 63] To check whether these heterostructures exhibit normal or relaxor ferroelectric behavior, we have fit the experimental data with equation (1) for 100 kHz (Fig. 4(b)). The values of γ were obtained from the slope of the graphs and δ values from the intercept of the curve based on:[60, 62, 63, 64]

$$\delta = \left(\frac{e^{-intercept}}{2\varepsilon_m}\right)^{1/\gamma} \qquad (3)$$

Figure 2 represents the variation of $ln\left(\frac{1}{\varepsilon_r} - \frac{1}{\varepsilon_m}\right)$ as a function of $ln(T - T_m)$ at a frequency of 100 kHz as representative of all the frequencies. The value of γ is determined to be 1.89 for 100 kHz and varies from 1.57 to 1.96 for the frequencies 1 kHz to 1 MHz. The higher value of γ, suggests more phase transition diffuseness with relaxor behavior. We obtained the value of $\delta \sim 83.84$ K for 100 kHz. This high diffusive parameter (δ) might be due to the strain experienced at different interfaces and mechanical coupling of the ferroelectric and magnetic layers. Different FE/FM composite structures have shown diffuse phase transition/relaxor type behavior.[29, 50] To further confirm this diffusive phase transition behavior, we have calculated

the degree of deviation (ΔT_m) from normal Curie Wiess law using the following equation[62, 64, 63, 65]

$$\Delta T_m = T_{cw} - T_m \qquad (4)$$

Where T_{CW} is the temperature where the dielectric permittivity starts to follow the curie Wiess law and the x-intercept of the $1/\varepsilon_r$ vs. T gives the Curie temperature value (T_C). The value of ΔT_m is 46 K for 100 kHz, which suggests broad relaxation behavior and further confirms the diffuseness of the phase transition and the relaxor ferroelectric nature of these heterostructures.

The variation of inverse of dielectric permittivity as a function of absolute temperature is useful to discern the order of the FE to paraelectric (PE) phase transition.[18, 66, 67] For a first order FE phase transition, when the Curie temperature approaches from below T_C the functionality follows:[18]

$$\frac{1}{\varepsilon_r} = 8\beta(Tc - T) + \frac{3\gamma^2}{4\delta}, T \rightarrow T_C^- \qquad (5)$$

and when Curie temperature approaches from above T_C:

$$\frac{1}{\varepsilon_r} = \beta(T - Tc) + \frac{3\gamma^2}{16\delta}, T \rightarrow T_C^+ \qquad (6)$$

For second order phase transition,

$$\frac{1}{\varepsilon_r} = \beta(T - Tc), T > Tc \quad \& \quad \frac{1}{\varepsilon_r} = 2\beta(Tc - T), T < Tc \qquad (7)$$

where T_C is the FE to PE transition temperature. Here β, δ, and γ are the coefficient in the Gibbs's free energy expansion.

The derivative $\xi = \frac{\partial}{\partial T}\left(\frac{1}{\varepsilon_r(T)}\right)$ changes from $\xi = \beta$ above T_C to $\xi = 2\beta$ below T_C for 2nd order phase transition.[18, 66]

Thus for the determination of the of order of the phase transition, $\xi (T)$ is important. As an example, we have plotted $1/\varepsilon$ versus T (left panel of Fig. 4(b)) *and* $\xi (T)$ versus T (right panel of Fig. 4(b)) for 100 kHz as space charge and interfacial polarization effects at low temperature can be avoided.[59] For high temperature PE phase ($T > 650$ K), $\xi \approx \sim 1.9343 \times 10^{-5}$ K^{-1} and lower temperature FE phase (T < 450 K), $\xi = -2.5209 \times 10^{-5}$ K^{-1} and is independent of temperature. The value of $\xi \approx 0$ corresponds to the ferroelectric T_C and for 100 kHz it is ~ 574 (+/- 5) K. Close to the phase transition temperature, $T \approx 570$ K, the derivative changes from $\zeta_1 = -3.93 \times 10^{-7}$ K^{-1} to $\xi \approx (4.6095 \times 10^{-7}$ K$^{-1})$ at $T \approx 580$ K and the derivative ratio (ζ_2/ζ_1) is found to be = -1.17. The change in the derivative ratio of -1.17 suggests these heterostructures undergo a 2nd order phase transition.[18, 66, 67]

PFN bulk ceramics exhibits FE T_C ~379-385 K, whereas PFN thin films have a ferroelectric T_C ~ 400, (+/- 5) K (at 100 Hz),[51] however we observe an increase in the ferroelectric T_C in these heterostructures, which might be due to the strain developed at different interfaces; shifts of hundred degrees in ferroelectric T_C in strained thin films has been reported previously.[36] It is theoretically predicted that the FE T_C can be increased to a maximum value about 4 times higher than that of the parent FE compound with increasing the concentration of magnetic material.[68] The coupling between the spins and charge at different interfaces can also shift the FE T_C.[22, 24, 33]

The tan δ (loss tangent) as a function of frequency of the multilayer heterostructures was measured at RT (inset of Fig. 4(a)). The tan δ value is found to be low and nearly constant up to 100 kHz then increases at higher frequency. The low loss tangent at RT makes these heterostructures suitable for many device applications.

We measured the electric field dependent polarization hysteresis loop of the PFN/NZFO/PFN/NZFO/PFN heterostructures at a frequency of 5 Hz at RT to investigate whether bulk ferroelectricity exists (Fig. 4(c)). The heterostructures exhibit highly resistive behavior and can withstand very high electric field. We observed well saturated ferroelectric heterostructures with saturation polarization (P_s) ~ 52 (+/-0.5) µC/cm^2, remnant polarization (P_r) ~ 29 (+/-0.5) µC/cm^2 and the coercive electric field (E_c) ~ 189.5 (+/-5) kV/cm. Pure PFN ceramics and thin films exhibit P_s ~ 30 µC/cm^2 and 57 µC/cm^2 respectively.[46, 51] The slight decrease of P_s in these heterostructures compared to pure PFN thin films might be due to the insertion of lower resistive NZFO layers. We observed a small asymmetry along the E-field axis, which might be due to the asymmetries between the LNO bottom electrode and the Pt top electrodes.[69] The asymmetry is also observed in the amplitude butterfly loop in the PFM measurements. Summarily, ferroelectric characteristics in these heterostructures are confirmed with the bulk and nanoscale measurements.

Magnetic Properties

The ferroelectric ordering temperature of PFN/NZFO/PFN/NZFO/PFN heterostructures has been observed above RT. To verify the multiferroicity in these heterostructures above RT we studied the temperature (T) and magnetic field (H) dependence of magnetization (Fig. 5(a,b)). Note that all the magnetic measurements were carried out in the in-plane configuration. Magnetization (M) as a function of T ($M(T)$) measurements were done in ZFC (zero field cooled) and FC (field cooled) by applying a dc magnetic field of ~ 0.1 T (Fig. 5(a)). No

significant bifurcation between FC and ZFC curves are observed as the applied magnetic field is larger than the coercive field of these nanostructures. We found the magnetization systematically decreases with increasing temperature and disappears above 600 K. We find the ferro(ferri) magnetic – paramagnetic T_C (transition temperature) of these heterostructures is ~ 585 (+/-10) K. Fig. 5(b) shows the H dependent magnetization ($M(H)$) measured at various temperatures. Initially the magnetization increases rapidly with up to 1.5 T then the slope decreases until it finally saturates completely. The magnetization decreases with increasing temperature. We observe perfectly saturated magnetization along with very low coercive field (H_c) for all temperatures indicating ferrimagnetic like behavior. The saturation magnetization (M_s) of these heterostructures at RT is ~ 62 (+/-1) emu/cm^3. The $M(H)$ loops recorded at ~ 700 K clearly indicates no magnetization above T_C.

PFN thin films and single crystals exhibit antiferromagnetic ordering below 170 - 200 K, however antiferromagnetic behavior below 150 K[17] and weak ferromagnetic ordering of PFN ceramics above RT has also been reported.[29, 70-74] Previously, we observed weak ferromagnetic/antiferromagnetic ordering in pure PFN thin films above RT and the ferrimagnetic - paramagnetic T_C of pure NZFO thin films ~ 713 K.[52] Here we observe enhanced magnetic T_C and magnetization of these heterostructures compared to PFN. This might be due to the coupling of the spins of NZFO and PFN at different interfaces and the strain developed due to lattice mismatch between different layers.[22, 24, 69] Magnetic T_C of the composite structures can be changed significantly if the magnetic material has negative values of magnetostriction (λ).[68] As NZFO is magnetostrictive and its parameters are negative (λ_s ~ -21.0 ×10^{-6}, λ_{100} ~ - 33.7×10^{-6}, λ_{111} ~ -13.2 ×10^{-6}), it favors the enhancement of T_C.[29, 50, 52] It is also theoretically studied that the value of polarization can modify the magnetic T_C remarkably.[68] The soft magnetic behavior (high M_s and low H_c) of these heterostructures make them suitable for different kinds of spintronic devices as low magnetization is desirable for low external field switching.[11, 54, 75]

Magnetoelectric Coupling Properties

PFN/NZFO/PFN/NZFO/PFN heterostructures display both the FE and magnetic T_C well above RT along with high magnetization and high polarization. We measured the parallel capacitance (C_p) of these multilayer heterostructures in a wide range of frequency (100 Hz – 1 MHz) at different static magnetic fields of ~ 0.5 and 1 T (Fig. 6) at RT to verify the existence of cross coupling between magnetic and electrical order parameters.[76] We find a significant decrease in capacitance with increasing magnetic field. The variation of capacitance with magnetic field

is found to be higher at lower frequency, which might be due to the absence of some types of polarizations dynamics (out of electronic, dipolar, space-charge/interfacial, and ionic polarization) at higher frequencies.[59] We computed the magneto-capacitance (MC %) of these nanostructures at different magnetic fields at selected frequencies (inset of Fig. 6). The MC % of these heterostructures at 1 kHz are found to be ~ - 2.69 and - 4.11 with the applied static H of 0.5 and 1 T respectively. The change of MC % is found to be less in the case of 1 T applied field compared to 0.5 T, which might be due to the nature of magnetic field dependence of magnetostriction.[14]

The ME coupling observed in our case might be due to different coupling mechanisms. First, strain developed (a) at different interfaces due to lattice mismatch and (b) by applying electric/ magnetic field because of inverse piezo electric/magnetic effect. The strain induced in the magnetic layer by the applied H transmits to the FE layers via the interface and by the piezoelectric effect, the strain changes the electrical order parameters. In these epitaxial heterostructures with sharp interfaces, the mechanical coupling among the FE and magnetic phases is notably strong due to near ideal transmission of mechanical strain.[19, 22, 29, 30, 33] The second reason for ME coupling is due to spin coupling between the MF (PFN) and magnetic (NZFO) layers, which causes the ionic displacement in both phases. Upon FE switching the interatomic distance between the magnetic cations at the interface is modified, which leads to a change in the exchange interaction and consequently couple the ferroic order parameters.[22, 24, 34] The third reason might be the charge coupling at the interface. The bound charge at the FE interface modifies the charge carrier density significantly in the magnetic layers via charge screening. This type of coupling avoids structural distortions and are reversible and non-volatile. In the solid state, charge density is an important fundamental quantity, as it can tune the electronic and magnetic properties of these nanostructures via electrostatic doping. Ultimately this enables sensitive control of the magnetic orderings, orbital state, electron correlations and transport properties.[24, 35, 55, 69, 77]

Conclusions

We have successfully synthesized phase pure PFN/NZFO/PFN/NZFO/PFN multilayer heterostructures by PLD. The presence of both phases and single crystalline quality has been confirmed from XRD and TEM studies. Local and global ferroelectricity in these nanostructures was confirmed by PFM and bulk ferroelectric hysteresis loop measurements. These multilayer heterostructures exhibit low dielectric loss, large polarization, and magnetization values at RT. These multilayer heterostructures exhibit 2nd order ferroelectric phase transition. The magnetic and ferroelectric T_C are determined to be well above RT. These

nanostructures show magnetodielectric coupling suggesting a strong coupling between the electrical and magnetic order parameters at RT. These multilayer heterostructures show room temperature multiferroicity along with strong magnetodielectric coupling, hence can be used in different (micro)nanoscale electronic, memory, and spintronic devices. This research will pave a path towards designing of new multilayer heterostructures to achieve large ME coupling at RT for envisioned devices.

Acknowledgments

Data Availability Statement:

The data that supports the findings of this study are available within the article [and its supplementary material].

Competing Interests:

The authors declare no competing financial and/or non-financial interest.

Figure Captions:

Fig. 1. (Color online) (a) Schematic diagram (b) XRD pattern at room temperature of PFN/NZFO/PFN/NZFO/PFN heterostructures.

Fig. 2. (Color online) **(**a) Cross-sectional high resolution TEM image (b) SAED patterns of PFN/NZFO/PFN/NZFO/PFN heterostructures.

Fig. 3. (Color online) (a) AFM topographic map, Band excitation PFM (b) phase image, **(**c) off-field phase (left panel) and amplitude (right panel) loop averaged over 5×5 grid of points (d) on-field (left panel) and off-field (right panel) piezoresponse hysteresis loop averaged over 5×5 grid of points of PFN/NZFO/PFN/NZFO/PFN heterostructures.

Fig. 4. (Color online) (a) Temperature dependent dielectric permittivity at selected frequencies (inset: frequency dependent loss tangent at RT) (b) Temperature dependent $1/\varepsilon_r$ (left panel) and ξ (right panel) (c) RT Ferroelectric hysteresis loop of PFN/NZFO/PFN/NZFO/PFN heterostructures.

Fig.   5.   (Color   online)   (a)   Temperature   dependent   magnetization   of

PFN/NZFO/PFN/NZFO/PFN heterostructures measured in ZFC and FC regimes with an applied static magnetic field of 1000 Oe (b) Magnetic field dependent magnetization (M-H) loops of PFN/NZFO/PFN/NZFO/PFN heterostructures at selected temperatures.

Fig. 6. (Color online) Frequency dependent parallel capacitance at different static magnetic field for PFN/NZFO/PFN/NZFO/PFN heterostructures at room temperature.
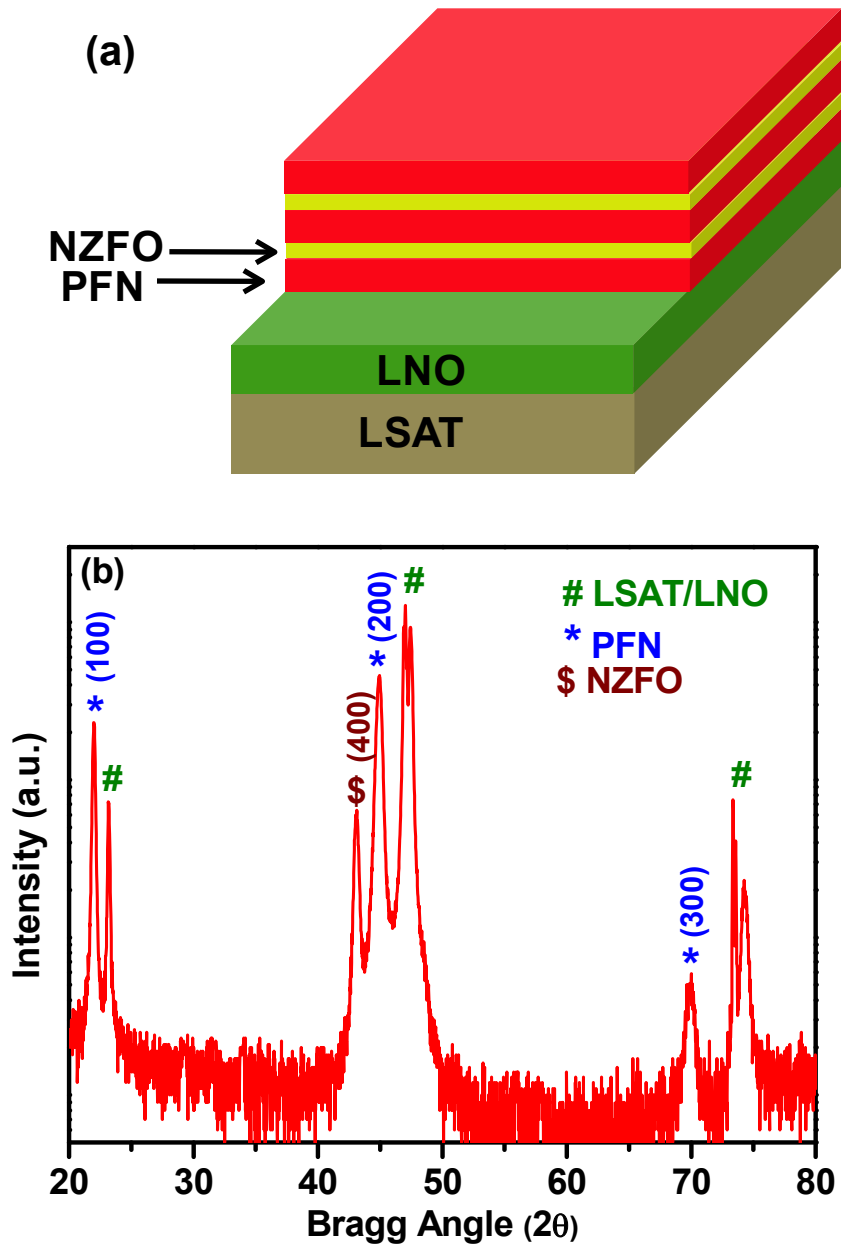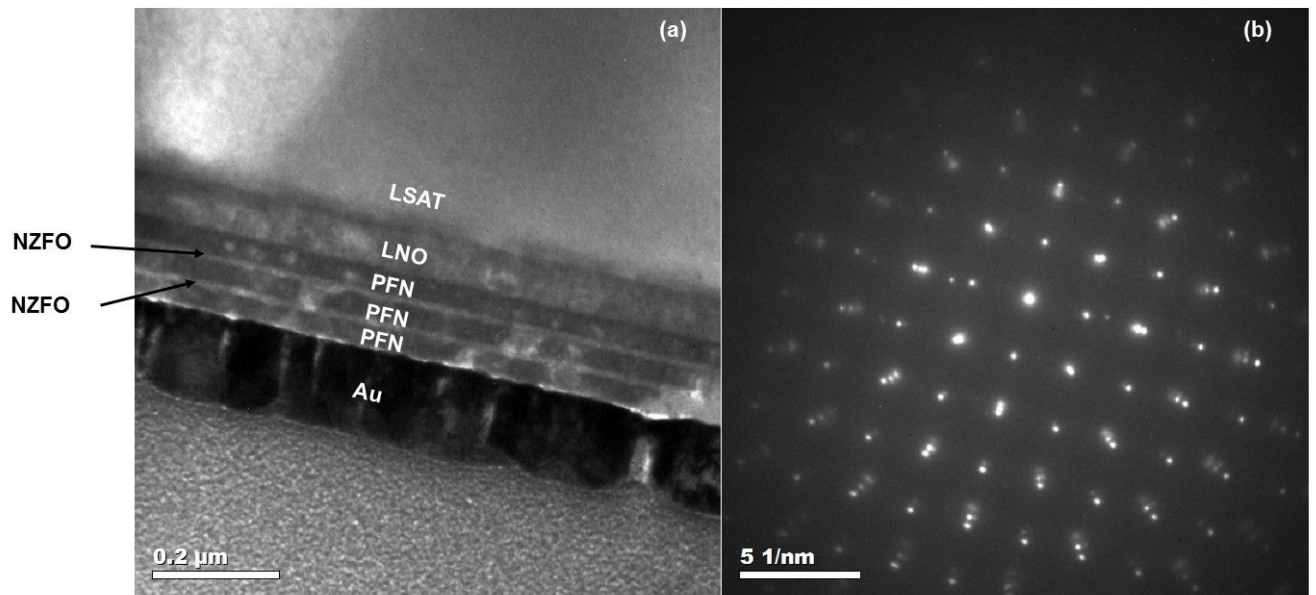
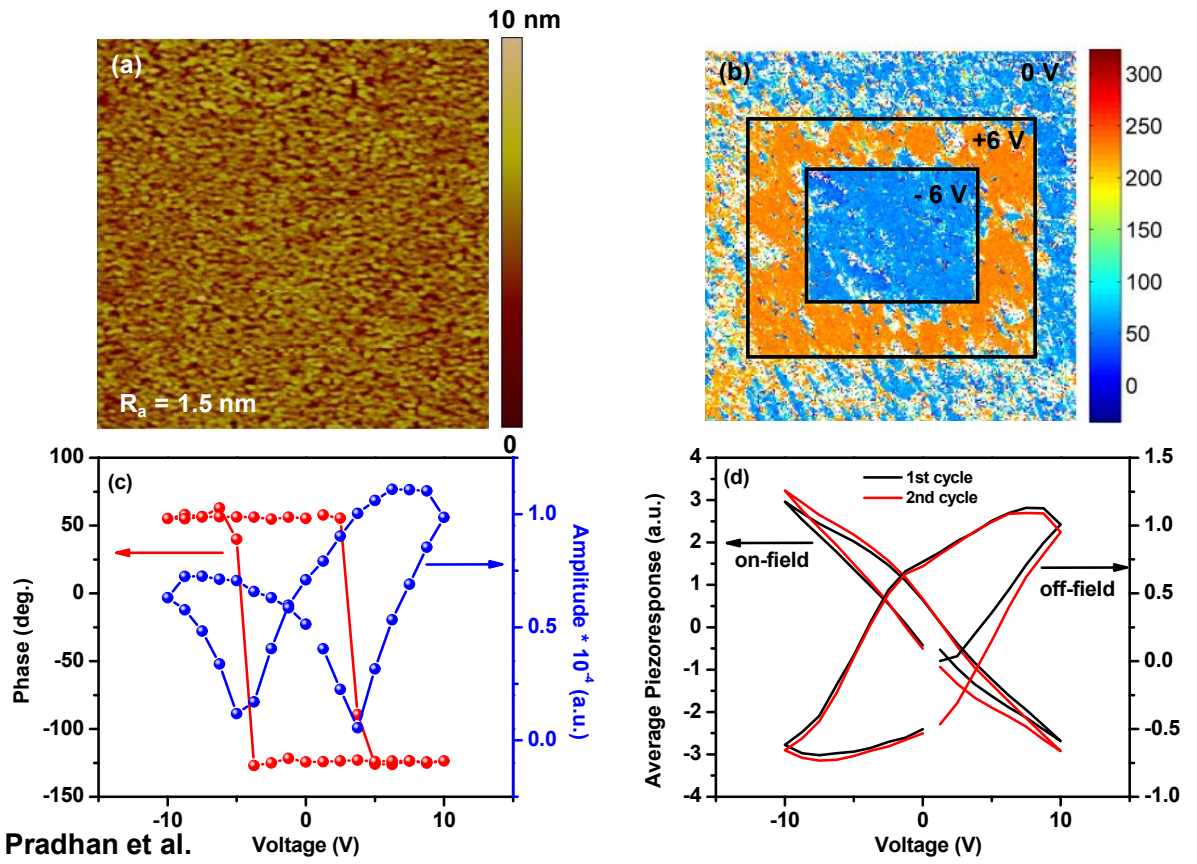**Figure 1. Pradhan et al.**

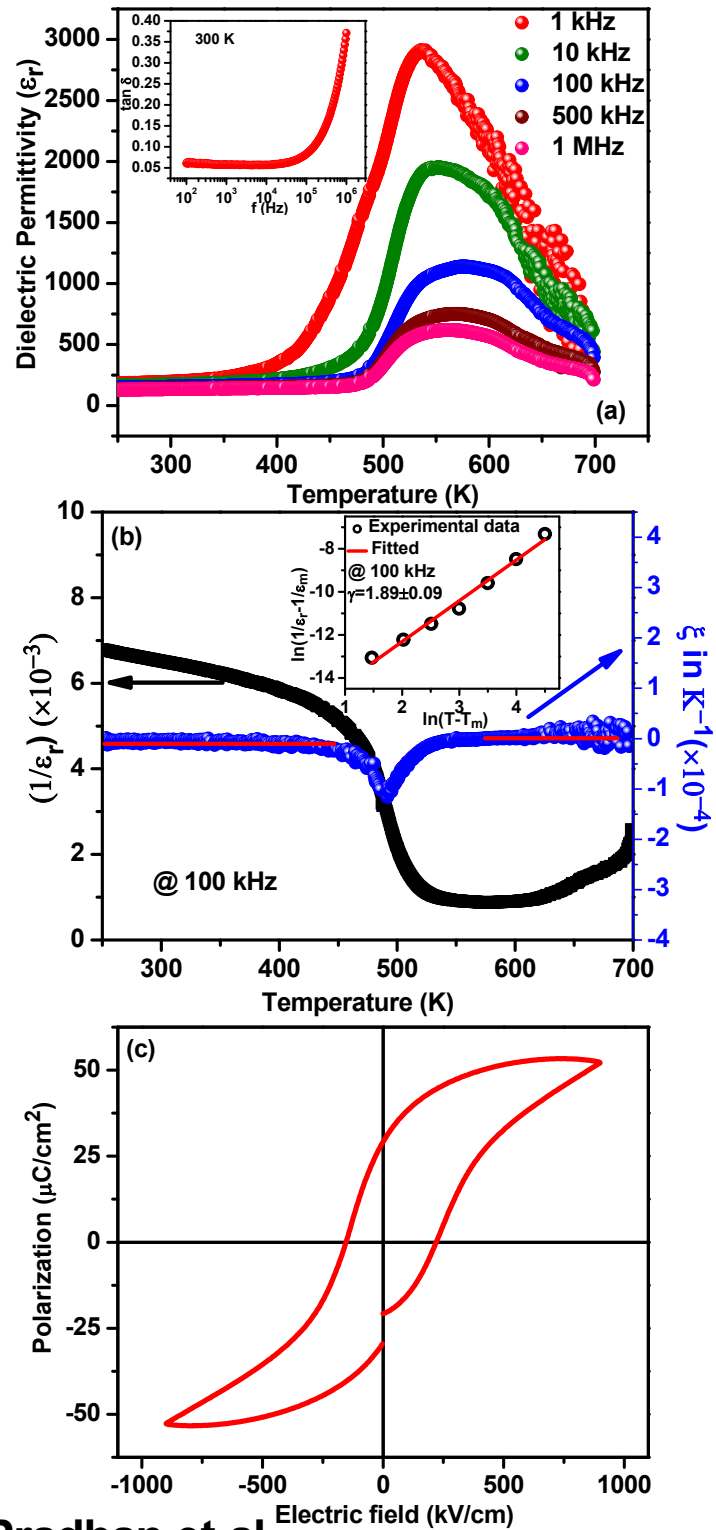**Figure 2. Pradhan et al.**

Figure 3. Pradhan et al.

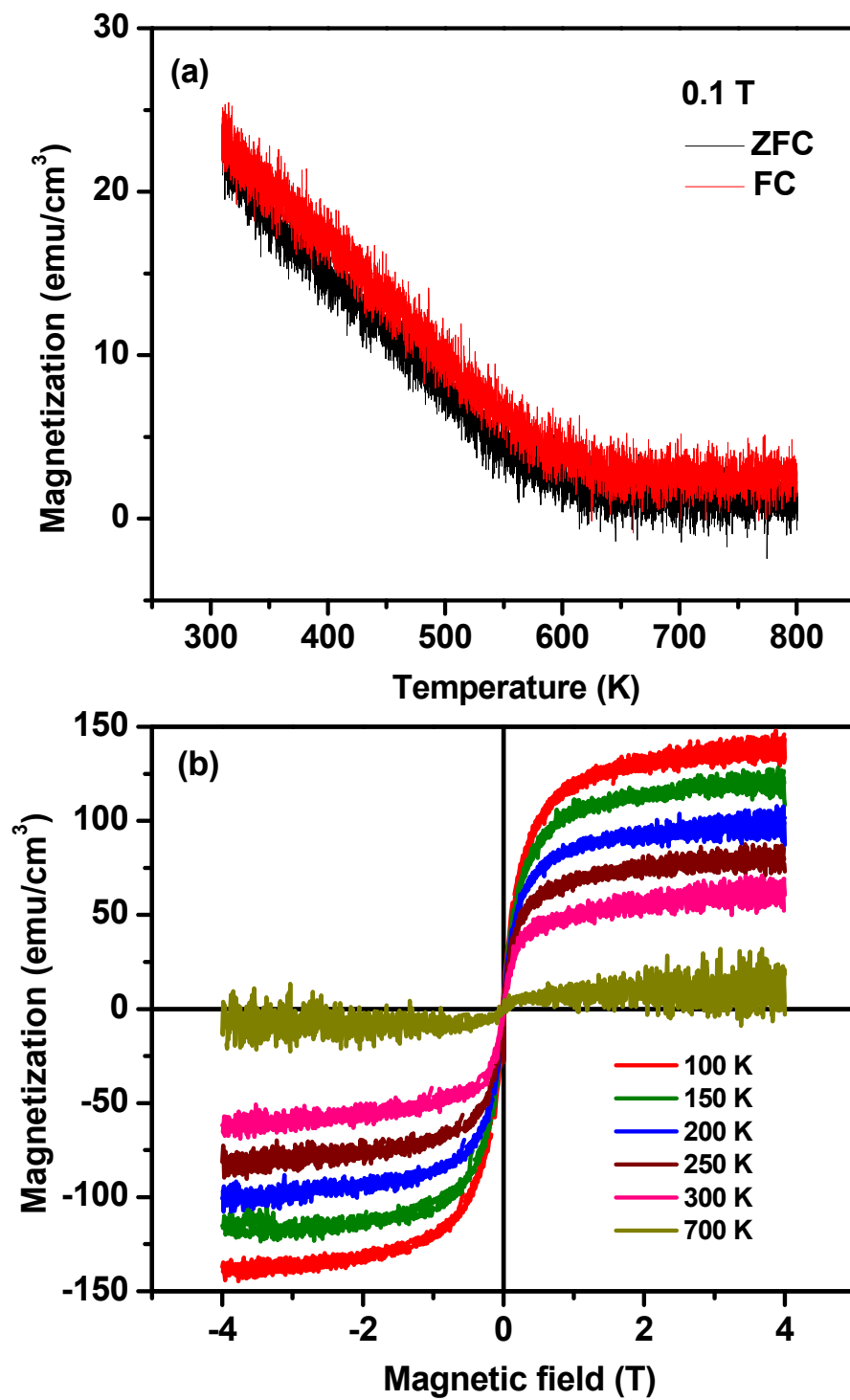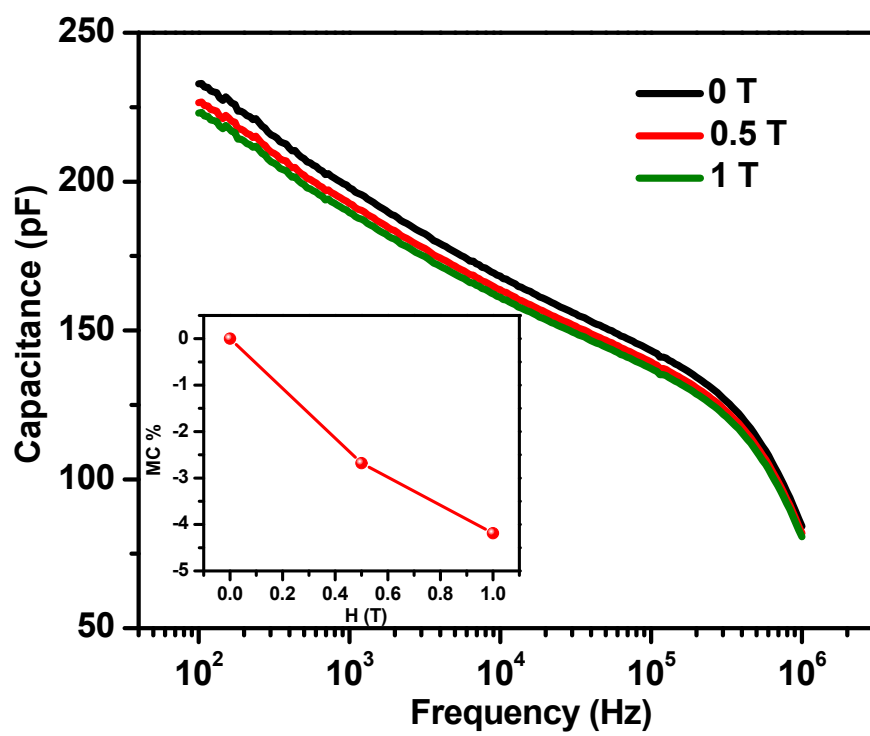**Figure 4. Pradhan et al.**

Figure 5. Pradhan et al.

Figure 6. Pradhan et al.

References:

1.   W. Eerenstein, N. Mathur and J. F. Scott, *nature*, 2006, **442**, 759-765.

2.   M. Fiebig, *Journal of physics D: applied physics*, 2005, **38**, R123.

3.   B. B. Van Aken, J.-P. Rivera, H. Schmid and M. Fiebig, *Nature*, 2007, **449**, 702-705.

4.   D. K. Pradhan, A. K. Mishra, S. Kumari, A. Basu, M. Somayazulu, E. Gradauskaite, R. M. Smith, J. Gardner, P. Turner and A. T. N'Diaye, *Scientific reports*, 2019, **9**, 1-12.

5.   H. Ohno, D. Chiba, F. Matsukura, T. Omiya, E. Abe, T. Dietl, Y. Ohno and K. Ohtani, *Nature*, 2000, **408**, 944-946.

6.   N. A. Spaldin and R. Ramesh, *Nature materials*, 2019, **18**, 203.

7.   J. Scott, *Nature materials*, 2007, **6**, 256-257.

8.   J. F. Scott, *NPG Asia Materials*, 2013, **5**, e72-e72.

9.   S. Manipatruni, D. E. Nikonov, C.-C. Lin, T. A. Gosavi, H. Liu, B. Prasad, Y.-L. Huang, E. Bonturim, R. Ramesh and I. A. Young, *Nature*, 2019, **565**, 35-42.

10.   M. Bibes and A. Barthélémy, *Nature materials*, 2008, **7**, 425-426.

11.   S. Fusil, V. Garcia, A. Barthélémy and M. Bibes, *Annual Review of Materials Research*, 2014, **44**, 91-116.

12.   N. A. Hill, *Journal*, 2000.

13.   L. Martin, Y.-H. Chu and R. Ramesh, *Materials Science and Engineering: R: Reports*, 2010, **68**, 89-133.

14.   C.-W. Nan, M. Bichurin, S. Dong, D. Viehland and G. Srinivasan, *Journal of applied physics*, 2008, **103**, 1.

15.   J. Ma, J. Hu, Z. Li and C. W. Nan, *Advanced materials*, 2011, **23**, 1062-1087.

16.   D. M. Evans, M. Alexe, A. Schilling, A. Kumar, D. Sanchez, N. Ortega, R. S. Katiyar, J. F. Scott and J. M. Gregg, *Advanced Materials*, 2015, **27**, 6068-6073.

17.   D. K. Pradhan, V. S. Puli, S. Kumari, S. Sahoo, P. T. Das, K. Pradhan, D. K. Pradhan, J. F. Scott and R. S. Katiyar, *The Journal of Physical Chemistry C*, 2016, **120**, 1936-1944.

18.   D. K. Pradhan, V. S. Puli, S. Narayan Tripathy, D. K. Pradhan, J. Scott and R. S. Katiyar, *Journal of Applied Physics*, 2013, **114**, 234106.

19.   Y. Wang, J. Hu, Y. Lin and C.-W. Nan, *NPG Asia Materials*, 2010, **2**, 61-68.

20.   J. Van Suchtelen, *Philips Res. Rep*, 1972, **27**, 28-37.

21.   Y. Li, Z. Wang, J. Yao, T. Yang, Z. Wang, J.-M. Hu, C. Chen, R. Sun, Z. Tian and J. Li, *Nature communications*, 2015, **6**, 1-7.

22. C. A. F. Vaz and U. Staub, *Journal of Materials Chemistry C*, 2013, **1**, 6731-6742.

23. V. Garcia, M. Bibes and A. Barthélémy, *Comptes Rendus Physique*, 2015, **16**, 168-181.

24. J.-M. Hu, C.-W. Nan and L.-Q. Chen, *Physical Review B*, 2011, **83**, 134408.

25. C. Lu, W. Hu, Y. Tian and T. Wu, *Applied physics reviews*, 2015, **2**, 021304.

26. R. Ranjith, B. Kundys and W. Prellier, *Applied Physics Letters*, 2007, **91**, 222904.

27. J. Xiong, T. Lei, J. Chu, C. Yang, J. Wei, M. Zhuo, E. M. Choi, B. Tao, W. Zhang and Y. Wang, *Small*, 2017, **13**, 1700107.

28. N. Ortega, A. Kumar, O. Resto, O. Maslova, Y. I. Yuzyuk, J. Scott and R. S. Katiyar, *Journal of Applied Physics*, 2013, **114**, 104102.

29. D. K. Pradhan, S. Kumari, R. K. Vasudevan, E. Strelcov, V. S. Puli, D. K. Pradhan, A. Kumar, J. M. Gregg, A. Pradhan and S. V. Kalinin, *Scientific reports*, 2018, **8**, 1-11.

30. H. Guo, Z. Wang, S. Dong, S. Ghosh, M. Saghayezhian, L. Chen, Y. Weng, A. Herklotz, T. Z. Ward and R. Jin, *Proceedings of the National Academy of Sciences*, 2017, **114**, E5062-E5069.

31. M. Singh, C. Simon, B. Raveau and W. Prellier, *Phase Transitions*, 2006, **79**, 973-990.

32. J. S. Andrew, J. D. Starr and M. A. Budi, *Scripta Materialia*, 2014, **74**, 38-43.

33. C. A. Vaz, J. Hoffman, C. H. Ahn and R. Ramesh, *Advanced Materials*, 2010, **22**, 2900-2918.

34. J. M. Hu, L. Q. Chen and C. W. Nan, *Advanced materials*, 2016, **28**, 15-39.

35. Z. Zhou, B. M. Howe, M. Liu, T. Nan, X. Chen, K. Mahalingam, N. X. Sun and G. J. Brown, *Scientific Reports*, 2015, **5**, 7740.

36. D. G. Schlom, L.-Q. Chen, C. J. Fennie, V. Gopalan, D. A. Muller, X. Pan, R. Ramesh and R. Uecker, *Mrs Bulletin*, 2014, **39**, 118-130.

37. T. Srinivasan, P. Ravindranathan, L. Cross, R. Roy, R. Newnham, S. Sankar and K. Patil, *Journal of Applied Physics*, 1988, **63**, 3789-3791.

38. T. Wu, A. Bur, K. Wong, J. Leon Hockel, C.-J. Hsu, H. K. Kim, K. L. Wang and G. P. Carman, *Journal of applied physics*, 2011, **109**, 07D732.

39. Z. Li, Y. Gao, B. Yang, Y. Lin, R. Yu and C. W. Nan, *Journal of the American Ceramic Society*, 2011, **94**, 1060-1066.

40. S. Rao, J. Prater, F. Wu, C. Shelton, J.-P. Maria and J. Narayan, *Nano letters*, 2013, **13**, 5814-5821.

41. L. You, C. Lu, P. Yang, G. Han, T. Wu, U. Luders, W. Prellier, K. Yao, L. Chen and J. Wang, *Advanced Materials*, 2010, **22**, 4964-4968.

42. N. Ortega, P. Bhattacharya, R. Katiyar, P. Dutta, A. Manivannan, M. Seehra, I. Takeuchi and S. Majumder, *Journal*, 2006.

43. R. Martínez, A. Kumar, R. Palai, G. Srinivasan and R. Katiyar, *Journal of Applied Physics*, 2012, **111**, 104104.

44. R. Kotnala, R. Gupta and S. Chaudhary, *Applied Physics Letters*, 2015, **107**, 082908.

45. A. Kumar, A. Goswami, K. Singh, R. McGee, T. Thundat and D. Kaur, *ACS Applied Electronic Materials*, 2019, **1**, 2226-2235.

46. A. Pavlenko, S. Shevtsova, A. Kozakov, L. Shilkina, A. Pavelko and L. Reznickenko, *Bulletin of the Russian Academy of Sciences: Physics*, 2012, **76**, 782-785.

47. D. Bochenek and P. Guzdek, *Journal of magnetism and magnetic materials*, 2011, **323**, 369-374.

48. D. K. Pradhan, P. Misra, V. S. Puli, S. Sahoo, D. K. Pradhan and R. S. Katiyar, *Journal of Applied Physics*, 2014, **115**, 243904.

49. D. K. Pradhan, S. K. Barik, S. Sahoo, V. S. Puli and R. Katiyar, *Journal of Applied Physics*, 2013, **113**, 144104.

50. D. K. Pradhan, S. Kumari, E. Strelcov, D. K. Pradhan, R. S. Katiyar, S. V. Kalinin, N. Laanait and R. K. Vasudevan, *npj Computational Materials*, 2018, **4**, 1-11.

51. D. K. Pradhan, S. Kumari, R. K. Vasudevan, S. Dugu, P. T. Das, V. S. Puli, D. K. Pradhan, S. V. Kalinin, R. S. Katiyar and P. D. Rack, *Journal of Applied Physics*, 2020, **127**, 194104.

52. D. K. Pradhan, S. Kumari, L. Li, R. K. Vasudevan, P. T. Das, V. S. Puli, D. K. Pradhan, A. Kumar, P. Misra and A. Pradhan, *Journal of Applied Physics*, 2017, **122**, 033902.

53. S. Jesse, R. Vasudevan, L. Collins, E. Strelcov, M. B. Okatan, A. Belianinov, A. P. Baddorf, R. Proksch and S. V. Kalinin, *Annual review of physical chemistry*, 2014, **65**, 519-536.

54. D. K. Pradhan, S. Sahoo, S. K. Barik, V. S. Puli, P. Misra and R. S. Katiyar, *Journal of Applied Physics*, 2014, **115**, 194105.

55. L. Martin and R. Ramesh, *Acta Materialia*, 2012, **60**, 2449-2470.

56. R. K. Vasudevan, N. Balke, P. Maksymovych, S. Jesse and S. V. Kalinin, *Applied Physics Reviews*, 2017, **4**, 021302.

57. S. V. Kalinin and A. Gruverman, *Scanning probe microscopy: electrical and electromechanical phenomena at the nanoscale*, Springer Science & Business Media, 2007.

58. N. Balke, P. Maksymovych, S. Jesse, A. Herklotz, A. Tselev, C.-B. Eom, I. I. Kravchenko, P. Yu and S. V. Kalinin, *ACS nano*, 2015, **9**, 6484-6492.

59. J. F. Nye, *Physical properties of crystals: their representation by tensors and matrices*, Oxford university press, 1985.

60. K. Uchino, *Ferroelectrics*, 1994, **151**, 321-330.

61. K. Uchino, *Ferroelectric devices*, CRC press, 2009.

62. T. Maiti, R. Guo and A. Bhalla, *Ferroelectrics*, 2011, **425**, 4-26.

63. K. Uchino and S. Nomura, *Ferroelectrics*, 1982, **44**, 55-61.

64. D. Viehland, S. Jang, L. E. Cross and M. Wuttig, *Physical Review B*, 1992, **46**, 8003.

65. S. Mahajan, O. Thakur, D. Bhattacharya and K. Sreenivas, *Materials Chemistry and Physics*, 2008, **112**, 858-862.

66. M. Tyunina, M. Plekh, M. Antonova and A. Kalvane, *Physical Review B*, 2011, **84**, 224105.

67. K. Datta, P. A. Thomas and K. Roleder, *Physical Review B*, 2010, **82**, 224105.

68. X. Lu, B. Wang, Y. Zheng and E. Ryba, *Journal of Physics D: Applied Physics*, 2007, **40**, 1614.

69. I. Fina, N. Dix, J. Rebled, P. Gemeiner, X. Marti, F. Peiro, B. Dkhil, F. Sanchez, L. Fabrega and J. Fontcuberta, *Nanoscale*, 2013, **5**, 8037-8044.

70. S. Majumder, S. Bhattacharyya, R. Katiyar, A. Manivannan, P. Dutta and M. Seehra, *Journal of applied physics*, 2006, **99**, 024108.

71. M. Carpenter, J. Schiemer, I. Lascu, R. Harrison, A. Kumar, R. Katiyar, N. Ortega, D. Sanchez, C. S. Mejia and W. Schnelle, *Journal of Physics: Condensed Matter*, 2015, **27**, 285901.

72. W. Kleemann, V. Shvartsman, P. Borisov and A. Kania, *Physical review letters*, 2010, **105**, 257202.

73. W. Peng, N. Lemée, J. Holc, M. Kosec, R. Blinc and M. Karkut, *Journal of magnetism and magnetic materials*, 2009, **321**, 1754-1757.

74. W. Peng, N. Lemée, M. Karkut, B. Dkhil, V. V. Shvartsman, P. Borisov, W. Kleemann, J. Holc, M. Kosec and R. Blinc, *Applied Physics Letters*, 2009, **94**, 012509.

75. S. Kumari, D. K. Pradhan, P. T. Das, N. Ortega, K. Pradhan, A. Kumar, J. Scott and R. S. Katiyar, *Journal of Applied Physics*, 2017, **122**, 144102.

76. R. Schmidt, J. Ventura, E. Langenberg, N. M. Nemes, C. Munuera, M. Varela, M. Garcia-Hernandez, C. Leon and J. Santamaria, *Physical Review B*, 2012, **86**, 035113.

77.   A. Sundararaj, G. Chandrasekaran, H. A. Therese and K. Annamalai, *Nanotechnology*, 2015, **26**, 315704.